L5/E5a-Based Fallback Mode for Dual-Frequency Multi-Constellation GBAS

Maria Caamano, Daniel Gerbeth, *German Aerospace Center (DLR)*

BIOGRAPHY

Maria Caamano received a Master's degree in Telecommunications engineering from the University of Oviedo, Spain, in March 2015, and a PhD in Aerospace Science and Technology from the Polytechnic University of Catalonia (UPC), Spain, in July 2022. Since May 2015, she has been working as a research associate at the Institute of Communications and Navigation at the German Aerospace Center (DLR). Her work focuses on the development of dual-frequency multi-constellation Ground Based Augmentation Systems (GBAS).

Daniel Gerbeth received his Bachelor's and Master's degrees in Electrical Engineering and Information Technology from the Karlsruhe Institute of Technology, Germany, in 2014. During his master studies he specialized in aerospace technology and navigation. After working in the field of sensor fusion and navigation aiding at Fraunhofer IOSB, he joined the German Aerospace Center (DLR) in May 2015 and has since been involved in research on Ground Based Augmentation Systems (GBAS) and reliable navigation for urban air mobility.

ABSTRACT

The future architecture for Dual-Frequency Multi-Constellation Ground-Based Augmentation Systems (DFMC GBAS), known as GBAS Approach Service Type (GAST) E, is designed to rely on measurements from two frequency bands, specifically L1/E1 and L5/E5a. However, unintentional Radio Frequency Interference (RFI) could affect one of the frequencies, typically L1/E1, potentially leaving GBAS with just a single operating frequency. In such a scenario, GAST E cannot function as intended, necessitating the definition of single-frequency fallback modes, either on L1/E1 or L5/E5a, to maintain CAT III service. Therefore, the definition of a GAST D-like mode based on L5/E5a becomes important. However, the integrity monitors designed for GAST D in current standards have only been validated for L1 and GPS and are known to be sensitive and trigger excessive false alarms when the ionosphere is very active. Therefore, in this paper, we evaluate the performance of a GAST D equivalent mode implemented for L5/E5a. The purpose of this study is to assess if this fallback mode can support CAT III operations, or whether the integrity monitors trigger excessive false alarms and consequently regular switches to a CAT I fallback mode can be expected. For these studies, we implement and adapt the main existing GAST D monitors for anomalous ionospheric gradient mitigation to operate in the L5/E5a frequency band. First, we assess the performance of these monitors under nominal conditions using real data collected by the Multipath Limiting Antennas (MLAs) installed at Tenerife Norte Airport and a user ground receiver located within the airport's protected area. Following the assessment under nominal conditions, we adapt the thresholds of these monitors and evaluate their performance using real data during scintillation events. Results show the need to adapt the monitors for L5/E5a and the suitability of the adapted thresholds to detect high ionospheric activity.

I. INTRODUCTION

The Ground Based Augmentation System (GBAS) is a local-area, airport-based augmentation of Global Navigation Satellite Systems (GNSS) that provides precision approach guidance for aircraft. GBAS enhances GNSS performance in terms of integrity, continuity, accuracy, and availability by providing differential corrections and integrity information to aircraft users. Differential corrections enable the aircraft to remove most of the spatially correlated errors between the ground station and the aircraft. Additionally, integrity parameters enable the airborne system to calculate bounds of the residual position errors and ensure the safety of the operation.

The GBAS Approach Service provides guidance on the final approach segment by outputting deviation information relative to a defined reference path. GBAS Approach Service Type C (GAST C) stations, which support operations under CAT I weather conditions, have been certified and are fully operational. Standards for GBAS Approach Service Type D (GAST D) stations, which are designed to support precision approaches and automatic landings down to CAT III weather conditions, have been agreed upon by the International Civil Aviation Organization (ICAO) at the end of 2016 (Radio Technical Commission for Aeronautics (2017)) and are in effect since November 2018. However, ground stations and avionics equipment are still under development. Both GAST C and GAST D are based on the use of the GPS constellation and the L1-frequency band only.

With the introduction of a second frequency (L5/E5a) usable for civil aviation and the development of multiple constellations (e.g. Galileo), new GBAS architectures and monitoring options have been proposed (Gerbeth et al. (2016)). One of the promising candidate architectures for Dual-frequency Multi-constellation (DFMC) GBAS was proposed in the framework of the Single European Sky ATM Research (SESAR) program in Europe. This candidate architecture (the so-called GAST F architecture in Durba (2018)), proposed to use 100-second smoothed pseudoranges on the L1/E1 frequency to compute the position of the aircraft and the second frequency (L5/E5a) for monitoring purposes. The main GAST F monitor that relied on the use of two frequencies was the dual-frequency airborne ionospheric gradient monitor (Gerbeth et al. (2022); Caamano et al. (2023)), which was used to detect satellites affected by anomalously large ionospheric gradients and exclude affected satellites from the position computation. In 2019, an alternative architecture, known as GAST X, was proposed in Murphy et al. (2021). GAST X proposed to send all relevant raw measurements to the aircraft and to use a divergence-free combination of L1/E1 and L5/E5a with a longer smoothing time constant for positioning. Similarly as described in Gerbeth et al. (2022), GAST X proposed to use both frequency bands for ionospheric monitoring as presented in Murphy et al. (2022).

In the most recent development, the ICAO GBAS Working Group (GWG), responsible for establishing standards for DFMC GBAS, has merged the previously distinct GAST F and GAST X architectures into a unified architecture known as GAST E. As part of this effort, architecture trade studies are underway to select the most suitable overall architecture and fallback modes and to formulate the concept of operation (ConOps) for DFMC GBAS. Notably, the newly introduced GAST E architecture retains the same ionospheric monitoring algorithms as initially proposed for both GAST F and GAST X and, consequently, its successful operation relies on the availability of two frequency bands: L1/E1 and L5/E5a.

However, although the L1/E1 and L5/E5a frequency bands used in aviation are regulated, unintentional Radio Frequency Interference (RFI), typically affecting one of the bands at a time, is occurring with increasing frequency as explained in Sokolova et al. (2022). This is due to the fact that GNSS is also used in other fields, such as tolls or asset tracking, where users may want to jam their own position in order to avoid certain controls. This is a problem especially for the GBAS ground station because, although it is located in protected locations within the airport area, GBAS receivers and antennas could be located very close to, e.g., busy roads, and therefore the probability of being affected by RFI is high.

Future GBAS architecture already foresee this problem and proposes fallback single-frequency modes in case one of the frequencies (L1/E1 or L5/E5a) is affected and becomes unavailable for all satellites. In case the L5/E5a frequency band becomes unavailable, GAST E can switch to the existing modes as follows: a switch to GAST D (CAT III) is triggered first and, if this mode is unavailable, a switch to GAST C (CAT I) is triggered (using two or more constellations instead of one if they are available). In case the L1/E1 frequency band becomes unavailable, both 30 seconds and 100 seconds smoothed pseudoranges for the L5/E5a frequency band will be available at the aircraft, enabling a fallback mode similar to GAST D for L5/E5 that, if available, uses multiple constellations instead of one. Thus, the "L5/E5a GAST D Equivalent Mode" supports CAT III operations. If this mode is unavailable, a switch to GAST C (CAT I) based on L5/E5a signals and multiple constellations if availabile would be triggered. However, as mentioned above, the ionospheric monitor used in GAST E relies on two frequencies. This means that this monitor cannot be used to detect and exclude satellites affected by anomalous ionospheric gradients in the L5/E5a-only modes. Therefore, alternative mitigation strategies must be designed and implemented for the L5/E5a-only modes since these anomalous ionospheric gradients can lead to hazardous position errors if they are not detected and mitigated (Pullen et al. (2009)).

In this paper, we evaluate the performance of the GAST D equivalent mode implemented for L5/E5a under both nominal ionospheric conditions and active ionospheric conditions (i.e. anomalous ionospheric gradients and/or scintillation affect one or several satellites). The purpose of this study is to assess if this fallback mode can support CAT III operations, or whether the monitors trigger excessive false alarms and consequently regular switches to the "L5/E5a GAST C equivalent mode" can be expected. For these studies, we implement and adapt the main existing GAST D monitors for anomalous ionospheric gradient mitigation, designed initially for the L1 frequency band as described in Pullen et al. (2017), to operate in the L5/E5a frequency band. In the case of the GBAS ground station, we consider the ground carrier-phase Ionospheric Gradient Monitor (typically referred to as IGM and initially described in Khanafseh et al. (2012)), and the ground Code-Carrier Divergence monitor (CCD) described in Pullen et al. (2017). At the airborne side, we consider the airborne version of the CCD and the Dual-Solution Ionospheric Gradient Monitoring Algorithm (DSIGMA), also described in Pullen et al. (2017). First, we assess the performance of these monitors under nominal conditions using real data collected by the Multipath Limiting Antennas (MLAs) installed at Tenerife Norte Airport and a user ground receiver located within the airport's protected area. Following the assessment under nominal conditions, we evaluate their performance using real data recorded at Tenerife Norte during scintillation events. These assessments and evaluations are conducted for dual-constellation scenarios involving both GPS and Galileo. At each stage, we compare the performance of "GAST D based on L5/E5a mode" with GAST D based on L1/E1.

The paper is structured as follows: Section II provides an overview of the main monitors considered in current GAST D standards, Section III describes the experimental setup installed at Tenerife Norte Airport, which was used to collect the measurements for this study, Section IV presents the monitors' performance in nominal conditions and the necessary adaptations for the monitors to function in the L5/E5a frequency band, and Section V presents the monitors' performance under active ionospheric conditions, and compares their performance with the monitors operating in the L1/E1 frequency band.

II. BACKGROUND

In this section, we provide a brief description of the primary monitors designed for ionospheric monitoring for GPS L1 as outlined in current GAST D standards.

1. Code-Carrier Divergence Monitor

The Code-Carrier Divergence (CCD) monitor detects and quantifies discrepancies between code and carrier-phase measurements received from the Global Navigation Satellite System (GNSS) satellites. Originally, this monitor was designed to detect satellite failures causing code and carrier-phase measurements to diverge. However, the monitor is also used to detect anomalously large ionospheric gradients (which also cause the code and carrier to diverge) preventing large differential position errors introduced by these gradients.

The CCD monitor is designed as two first order Linear Time Invariant (LTI) cascaded filters operating on the difference of the code-minus-carrier measurements as:

$$d_r^n(t) = \frac{|\rho_r^n(t) - \phi_r^n(t)| - |\rho_r^n(t-1) - \phi_r^n(t-1)|}{\Delta t}, \tag{1}$$

$$Z_r^n(t) = \left(1 - \frac{\Delta t}{\tau}\right) \cdot Z_r^n(t-1) + \frac{\Delta t}{\tau} \cdot d_r^n(t), \tag{2}$$

$$D_r^n(t) = \left(1 - \frac{\Delta t}{\tau}\right) \cdot D_r^n(t-1) + \frac{\Delta t}{\tau} \cdot Z_r^n(t), \tag{3}$$

where $\rho_r^n(t)$ is the raw pseudorange measurement in meters at epoch t for satellite n and reference receiver r, $\phi_r^n(t)$ is the carrier-phase measurement in meters at epoch t for satellite n and reference receiver r, Δt is the time difference between two consecutive epochs, $Z_r^n(t)$ is the filter state at epoch t, and $D_r^n(t)$ is the filter output at epoch t.

In the final validation of the ICAO requirements for GAST D operating on GPS L1 (Pullen et al. (2017)), a smoothing time constant of 25 seconds was selected for τ, and the monitoring threshold was derived to be 40.78 mm/s based on a defined discriminator noise sigma of 6.9 mm/s and an allocated false detection probability of $3.4 \cdot 10^{-9}$. The equation to compute the detection threshold is:

$$T_{CCD} = K_{FD} \cdot \sigma_{CCD}, \tag{4}$$

where K_{FD} is the false detection multiplier corresponding to the previously allocated probability of false detection, and σ_{CCD} is the discriminator noise sigma.

The CCD monitoring was also introduced into the airborne system in GAST D. However, different values for the time constants and the threshold were defined. In this case, the airborne CCD time constants were set to 100 seconds and its threshold was defined to be sightly larger than that of the ground (41.50 mm/s).

Both monitors, ground and airborne CCD, are effective in detecting fast moving ionospheric gradients. If the monitor's predefined threshold is exceeded, the affected satellite is temporarily excluded from the processing at the ground station and from the computation of the GAST D position solution on the airborne side. The possibility of reintroducing these satellites into the system is subject to different criteria for ground and airborne CCD, and can be found in Pullen et al. (2017).

2. Ground Ionospheric Gradient Monitor

The ground Ionospheric Gradient Monitor (IGM), as it was developed for GBAS, uses double difference carrier-phase measurements between the known Multipath Limiting Antenna (MLA) baselines to directly observe the effect of the ionospheric anomalies. The algorithm models the ionospheric front as a slant gradient and assumes that the baselines between the antennas in the GBAS ground station are aligned with the runway. In this section, we provide a brief overview of how this monitor operates, while more comprehensive information regarding its definition and implementation is available in the original publication by Khanafseh et al. (2012).

The test statistic of this monitor can be defined as:

$$s_{r,k}^{n,m}(t) = \Delta^2\phi_{r,k}^{n,m}(t) - (\boldsymbol{\Delta e_{r,k}^{n,m}})^{\boldsymbol{T}}\boldsymbol{(t)} \cdot \boldsymbol{x_b} - \lambda \cdot round\left(\frac{\Delta^2\phi_{r,k}^{n,m}(t) - (\boldsymbol{\Delta e_{r,k}^{n,m}})^{\boldsymbol{T}}\boldsymbol{(t)} \cdot \boldsymbol{x_b}}{\lambda}\right), \tag{5}$$

where $\Delta^2\phi_{r,k}^{n,m}(t)$ is the double carrier-phase difference between two satellites (the satellite to monitor, n, and a reference satellite that is assumed to be bias-free, m) and two reference antennas (r and k), $(\boldsymbol{\Delta e_{r,k}^{n,m}})^{\boldsymbol{T}}\boldsymbol{(t)}$ is the transpose vector that represents the difference between user-satellite unit line of sight vectors for satellites n and m and antenna locations r and k, $\boldsymbol{x_b}$ is the baseline vector between antennas r and k, and λ is the carrier-phase wavelength. Note that vectors are expressed in bold letters. The product between two scalars is expressed with a dot ($\cdot$) and the scalar product between two vectors is expressed also with a dot ($\cdot$).

Under fault free conditions, this test statistic has a zero mean and a standard deviation of σ_s. Given an acceptable false detection probability under fault free conditions, P_{FD}, and the equivalent false detection multiplier, K_{FD}, computed as the inverse of the standard normal cumulative distribution function, a detection threshold can be defined as:

$$T_{IGM} = \frac{K_{FD} \cdot \sigma_s}{\|\boldsymbol{x_b}\|}. \tag{6}$$

A minimum detectable error for this monitor can be defined if the probability of missed detection, P_{MD}, is also considered. The minimum detectable error is the value above which all anomalous gradients will be detected with a probability of $(1 - P_{MD})$ and can be computed as:

$$MinDE = \frac{(K_{FD} + K_{MD}) \cdot \sigma_s}{\|\boldsymbol{x_b}\|}. \tag{7}$$

However, due to the fact that full cycles are removed in Equation 5, the resulting test statistic is bound between ± 0.5 cycles (scaled by the baseline). At some point, an error exceeding a certain slope cannot be distinguished anymore from another phase cycle along the baseline, leading to an upper bound at which a detection is ensured. Therefore, a maximum detectable error can be defined as:

$$MaxDE = \frac{\lambda \pm (K_{FD} + K_{MD}) \cdot \sigma_s}{\|\boldsymbol{x_b}\|}. \tag{8}$$

The performance of the monitor considering different baseline lengths and different noise levels for the differential carrier phase measurements can be found in Khanafseh et al. (2012). The values proposed in the standards for P_{FD} and P_{MD} are $3 \cdot 10^{-8}$ and $1 \cdot 10^{-9}$ respectively as stated in Pullen et al. (2017).

3. Dual-Solution Ionospheric Gradient Monitoring Algorithm

The Dual-Solution Ionospheric Gradient Monitoring Algorithm (DSIGMA) computes the difference between the corrected 30 seconds and 100 seconds smoothed pseudoranges and compares it with a certain threshold.

The test statistic of this monitor is defined as:

$$\rho_{DIFF}(t) = \overline{\rho}_{air,corr,100}(t) - \overline{\rho}_{air,corr,30}(t), \tag{9}$$

with

$$\overline{\rho}_{air,corr}^{n}(t) = \overline{\rho}_{air}^{n}(t) + PRC_{TX}^{n}(t_{PRC}) + RRC_{TX}^{n}(t - t_{PRC}) + TC_{air}^{n}(t) + c \cdot \delta t^{n}(t), \tag{10}$$

where $\overline{\rho}_{air}^{n}(t)$ is the airborne smoothed pseudorange for the satellite n at current epoch t, PRC_{TX}^{n} is the broadcast correction at time t_{PRC}, RRC_{TX} is the range rate correction broadcast at time t_{PRC}, TC_{air}^{n} is the differential tropospheric correction, δt^{n} is the clock bias for satellite n computed by the airborne receiver, and c is the speed of light.

The threshold for this monitor can be computed as:

$$T_{DSIGMA} = K_{FD} \cdot \sigma_{DSIGMA}, \quad (11)$$

where K_{FD} represents the false detection multiplier (with a value of 5.61 as documented in Pullen et al. (2017)), and σ_{DSIGMA} denotes the standard deviation of the distribution that overbounds the tails of the distribution formed by the test statistics of this monitor. The final threshold value for current GAST D standards (based on GPS L1) was established at 0.976 meters in Pullen et al. (2017).

III. EXPERIMENTAL SETUP

For the evaluations carried out in this work, we utilized data obtained from a research installation situated at Tenerife Norte Airport. Tenerife Norte is situated at a latitude of 28.48°, which can be considered an equatorial region. Consequently, the results obtained using data collected at this installation may differ from what is typically observed in GAST D based on GPS L1 measurements collected at mid-latitudes.

This installation consists of three Dual-frequency Multi-constellation (DFMC) Multipath Limiting Antennas (MLAs) located in close proximity to the runway (identified as RX1, RX2, and RX3 in Figure 1) and a user ground receiver equipped with a Pinwheel DFMC antenna (depicted in red in Figure 1). The distances between the different antennas are as follows: 0.2 km between RX1 and RX2, 1.05 km between RX2 and RX3, 1.25 km between RX1 and RX3, and 2.67 km between RX1 and the user.

Figure 1: Experimental setup installed at Tenerife Norte Airport. The blue markers represent the location of three ground reference antennas, and the red marker the location of the ground user receiver.

For the evaluations conducted under nominal conditions, we utilized data collected on the 21st of October 2022, when the ionospheric conditions were nominal during the vast majority of the time. The periods of time that were considered abnormal (containing scintillation or ionospheric irregularities) were removed from this data set before processing it. Figure 2a, shows the L1/E1 slant ionospheric delays computed for this day and one of the ground reference receivers (RX1) using dual-frequency carrier-phase measurements. As can be observed, the slant ionospheric delays do not present any irregularities or jumps indicating scintillation and can be considered to be in nominal conditions. The vertical offsets observable in Figure 2a are due to the unresolved carrier-phase ambiguities present in the carrier-phase measurements used to estimate the slant ionospheric delays.

For the evaluations conducted under active ionospheric conditions, we employed data collected on the 18th of November 2022. Figure 2b shows the L1/E1 slant ionospheric delays computed for this day and one of the ground reference receivers (RX1) using dual-frequency carrier-phase measurements. On this particular day, there were several instances of small-scale ionospheric irregularities during the nighttime and several satellites were affected by scintillation after sunset.

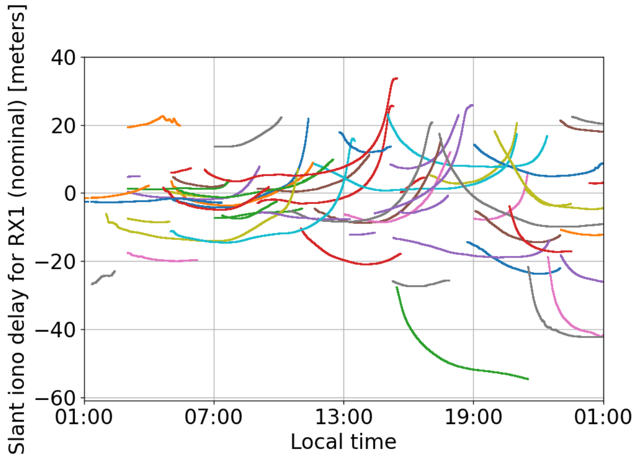

(a) Nominal conditions.

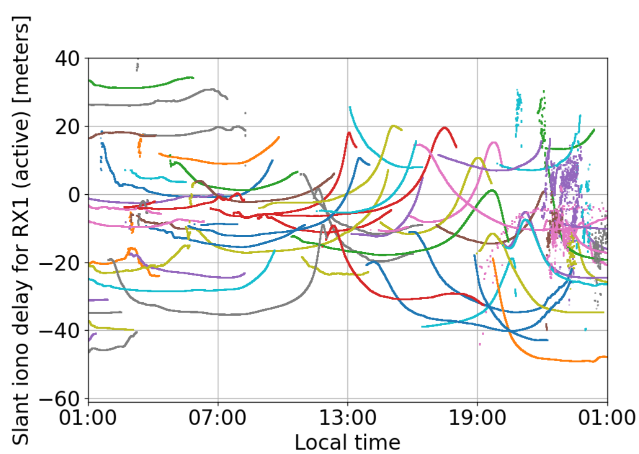

(b) Active conditions.

Figure 2: Slant ionospheric delays computed for L1/E1 and ground reference receiver RX1.

IV. EVALUATION OF THE MONITORS IN NOMINAL CONDITIONS AND PROPOSED ADAPTATIONS

In this section, we evaluate the performance of the monitors described in Section II for both the L1/E1 and the L5/E5a frequency bands and nominal conditions.

1. Ground Code-Carrier Divergence Monitor

This section presents the results of the evaluation of the ground CCD monitor in nominal conditions (i.e., no anomalous ionospheric gradients and/or scintillation are present in the measurements). Initially, we assessed the CCD monitor's performance using the L1/E1 GPS and Galileo data collected at Tenerife Norte to confirm that the CCD sigma noise discriminator, computed with this specific dataset from this installation, aligned with the value described in the current GAST D standards for GPS L1.

As a first step, we computed the test statistic of the monitor for every epoch as described in Equation 3. Then, we normalized the test statistics by subtracting from each sample the mean of the distribution formed by all test statistic samples and dividing the resulting values by the standard deviation of this distribution. Figure 3a shows with blue dots the Cumulative Distribution Function (CDF) of the normalized test statistic distribution, as well as its complementary function (1-CDF). Typically, the normalized test statistic distribution is assumed to follow a Gaussian distribution but, as can be observed in Figure 3a, the actual distribution of the normalized test statistics, represented in blue dots, was above the normal distribution $\mathcal{N}(0,1)$ in the tails, represented by the black dot-dashed line. Therefore, inflation was needed in order to protect the tails of the distribution. This inflation is represented by the green dashed line in Figure 3a, which corresponds to a $\mathcal{N}(0,\sigma_{CCD,L1})$. Therefore, we obtained an inflated sigma noise discriminator for the CCD monitor on L1/E1, GPS and Galileo and RX1 of 6.64 mm/s. We repeated the same process using the nominal data collected with ground reference receivers RX2 and RX3, and obtained as a result inflated sigma noise discriminators of 6.36 mm/s and 6.58 mm/s, respectively. These values are below the 6.9 mm/s limit described in the standards and, therefore, we can conclude that the data collected in Tenerife Norte for GPS and Galileo and the L1/E1 frequency band fulfilled the requirements in the standards for GAST D GPS L1.

As a second step, we evaluated the CCD's performance with the L5/E5a and GPS and Galileo data collected at Tenerife Norte. This evaluation aimed to determine whether the threshold specified in the GAST D standards remains applicable for a CCD monitor operating in the L5/E5a frequency band. Figure 3b depicts the tail overbounding process for RX1. As can be observed, the tails of the distribution needed also to be overbounded, giving a total inflated noise sigma discriminator of 8.51 mm/s for ground reference receiver RX1. For ground reference receivers RX2 and RX3, we obtained values of 8.54 mm/s and 8.36 mm/s, respectively. As these values are well above the 6.9 mm/s limit described in the GAST D standards, these results suggest that the threshold for this monitor should be adapted to operate in the L5/E5a frequency band.

To achieve this, we considered the highest value of the CCD inflated discriminator noise sigma among the three ground reference receivers for L5/E5a while maintaining the same probability of false detection specified in the GAST D standards (see Section II.1). Through the application of Equation 4, we derived a new threshold value of 50.47 mm/s. In Section V.1, we tested this adapted threshold for L5/E5a with data collected during periods of high ionospheric activity to ensure its effectiveness in detecting anomalous ionospheric irregularities.

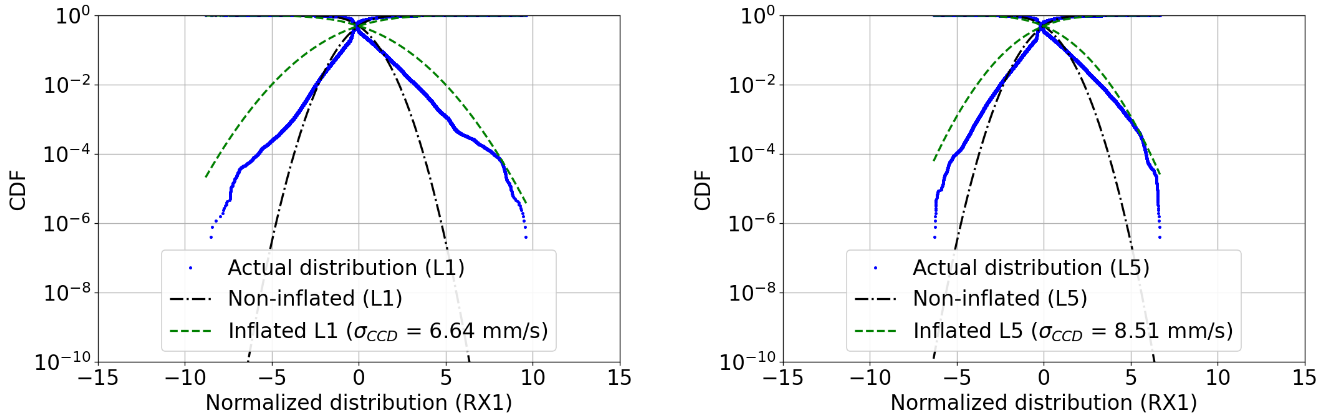

(a) L1/E1 and reference receiver RX1.

(b) L5/E5a and reference receiver RX1.

Figure 3: Cumulative Distribution Function and its complementary function depicted for the normalized CCD test statistic distributions (blue dots) and reference receiver RX1. The black dot-dashed line represents the non-inflated Gaussian distribution and the dashed green line represents the inflated Gaussian distribution.

2. Ground Ionospheric Gradient Monitor

This section presents the results of the evaluation of the IGM under nominal conditions. Similar to the previous section, the initial assessment of IGM's performance involved the use of L1/E1 GPS and Galileo data collected at Tenerife Norte. This evaluation aimed to compare its performance against the values stipulated in the current GAST D standards. Note that we conducted this evaluation exclusively for the baseline between RX1 and RX2, located around 200 meters away.

Figure 4a depicts the test statistics computed according to Equation 5 using an elevation mask of $5°$. As can be observed, there were certain satellites that presented higher nominal slant ionospheric delays than others. These observable trends were associated with satellites either raising above the elevation mask or descending, soon to be below it. Furthermore, the values of the nominal slant ionospheric delays for these low elevation satellites were larger than the typical values for slant ionospheric delays obtained for the same elevations at mid-latitude locations, highlighting the fact that Tenerife Norte's location can be considered within the equatorial region.

In order to better observe the values of the IGM test statistics over time, we applied an elevation mask of $15°$. As a result, the highest values of nominal slant ionospheric delays mentioned previously were not visible anymore, as depicted in Figure 4b. In this case, however, a distinct residual wave pattern became more apparent. As explained in Khanafseh et al. (2012), this pattern arises from the differences in phase patterns from the MLAs, leading to an error in the IGM test statistics. This error needs to be characterized and calibrated to optimize IGM's performance.

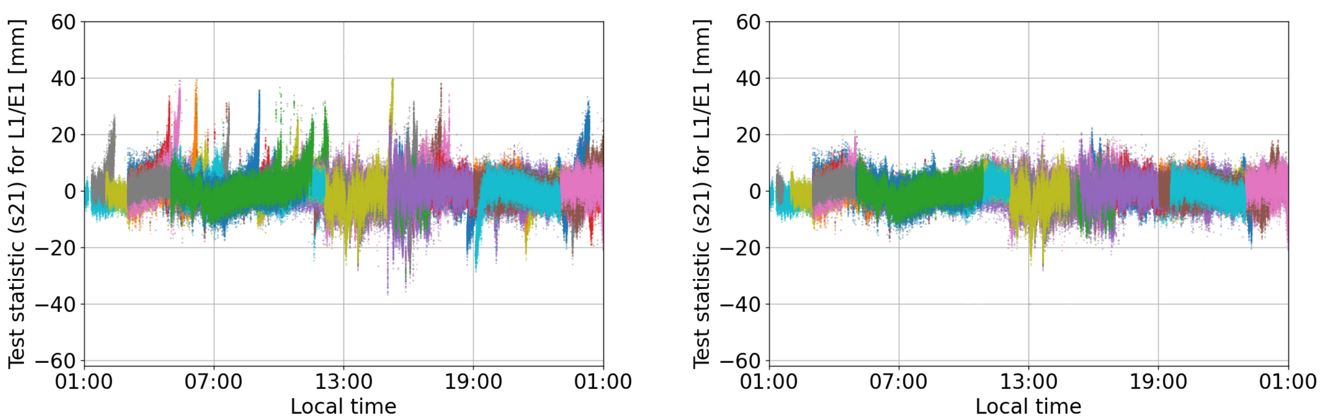

(a) L1/E1 and 5° elevation mask.

(b) L1/E1 and 15° elevation mask.

Figure 4: IGM test statistics computed for L1/E1 and different elevation masks.

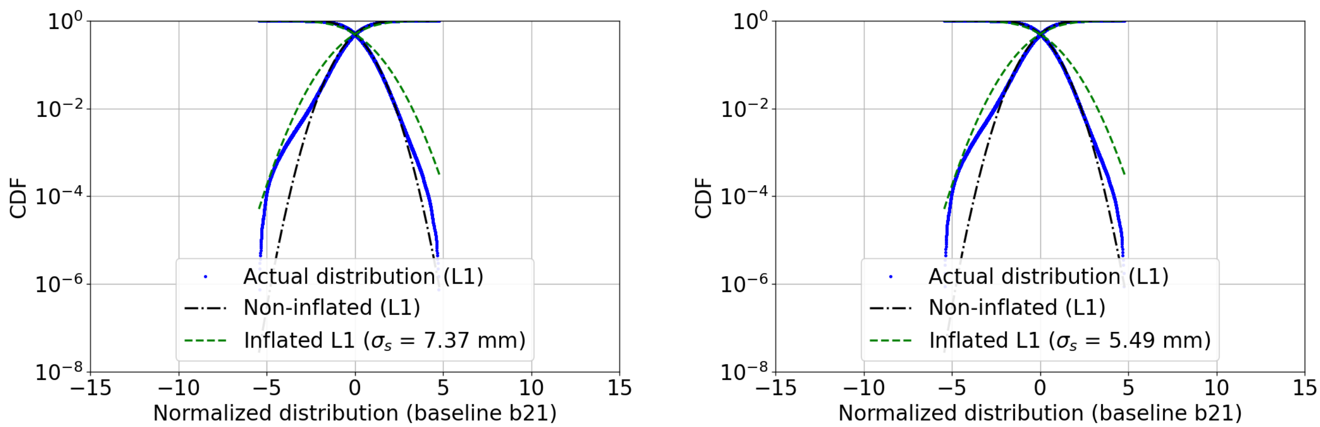

(a) L1/E1 and 5° elevation mask.

(b) L1/E1 and 15° elevation mask.

Figure 5: Cumulative Distribution Function and its complementary function depicted for the normalized IGM test statistic distributions (blue dots) and different elevation masks. The black dot-dashed line represents the non-inflated Gaussian distribution and the dashed green line represents the inflated Gaussian distribution.

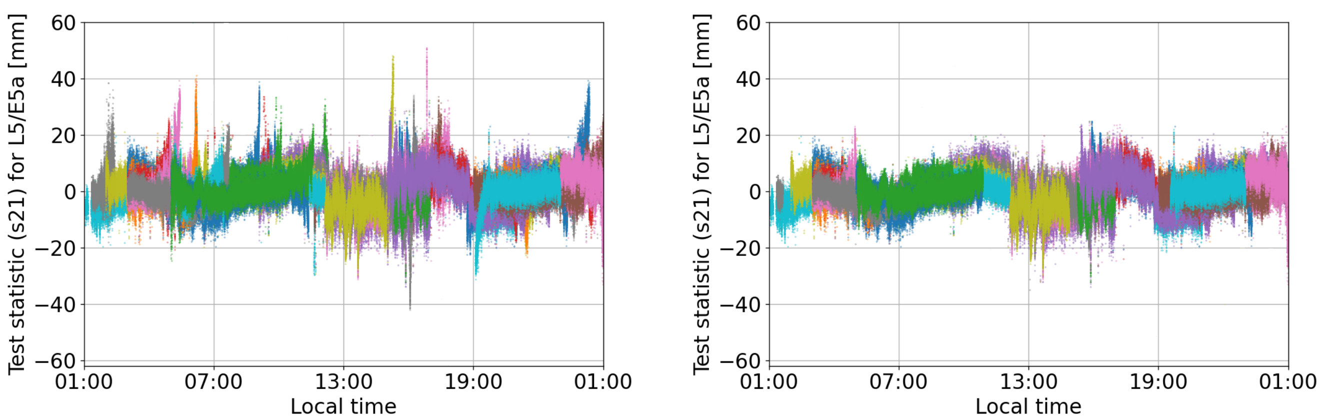

(a) L5/E5a and 5° elevation mask.

(b) L5/E5a and 15° elevation mask.

Figure 6: IGM test statistics computed for L5/E5a and different elevation masks.

Following the same procedure as in the previous section, we computed the inflated standard deviations for IGM, employing the two aforementioned elevation masks. The value obtained when considering all satellites above 5° was 7.37 mm as can be observed in Figure 5a, while Figure 5b illustrates that this value can be reduced to 5.49 mm when applying an elevation mask of 15°. This latter value aligns more closely with typical values for MLAs in the GAST D standards, typically ranging between 3 mm and 6 mm (Khanafseh et al. (2012)).

Subsequently, Figures 6a and 6b present the IGM test statistics computed for L5/E5a using 5° and 15° elevation masks, respectively. Correspondingly, Figures 7a and 7b present the inflated standard deviations associated with these test statistics while employing the same elevation masks. When using a 5° elevation mask, the inflated sigma computed for L5/E5a was slightly higher than that of L1/E1. This is attributed to the fact that slant ionospheric delays for L5/E5a are typically higher than those for L1/E1. Furthermore, when applying the 15° elevation mask, we observed that the inflated standard deviation remained considerably larger than that of L1/E1. This outcome can be attributed to the more pronounced characteristic wavy pattern associated with L5/E5a. This effect is attributed to the optimization of MLAs for the L1/E1 frequency band, making them less optimized for L5/E5a.

Next, we computed the thresholds, and minimum and maximum detectable errors for this baseline according to Equations 6, 7, and 8. Table 1 presents the results of these values for L1/E1 and L5/E5a while applying different elevation masks. As can be observed in Table 1, the threshold values for L5/E5a considering a probability of false detection of $3.0 \cdot 10^{-8}$ as in Pullen et al. (2017) are slightly higher than those for L1/E1 due to the correspondingly higher inflated standard deviation values.

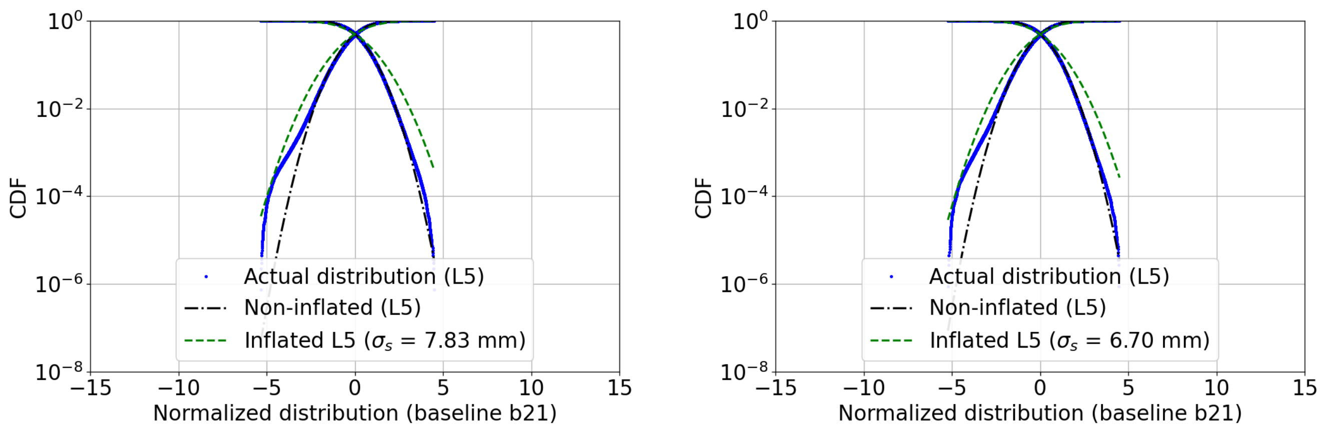

(a) L5/E5a and 5° elevation mask.

(b) L5/E5a and 15° elevation mask.

Figure 7: Cumulative Distribution Function and its complementary function depicted for the normalized IGM test statistic distributions (blue dots) and different elevation masks. The black dot-dashed line represents the non-inflated Gaussian distribution and the dashed green line represents the inflated Gaussian distribution.

When considering also the probabilities of missed detection of the monitor ($1 \cdot 10^{-9}$ as in Pullen et al. (2017)), we observe a significantly wider detectability range (values between the minimum detectable error and the maximum detectable error) for L5/E5a as compared to L1/E1. The reason behind is that the maximum detectable error value is wavelength-dependent, as explained in Equation 8. Therefore, despite the slightly higher value of the minimum detectable error due to the higher inflated standard deviation, we can expect to detect a wider range of gradient slopes with the monitor implemented for L5/E5a than for L1/E1, especially if antenna errors are calibrated.

Table 1: Detection thresholds, and minimum and maximum detectable error values for IGM.

Elevation mask	**5°**	**15°**
σ_s L1/E1 [mm]	7.37	5.49
σ_s L5/E5a [mm]	7.83	6.70
T_{IGM} L1/E1 [mm/km]	204.14	152.07
T_{IGM} L5/E5a [mm/km]	216.89	185.59
Detectability range L1/E1 [mm/km]	425.25 - 527.25	316.77 - 635.73
Detectability range L5/E5a [mm/km]	451.79 - 822.21	386.59 - 887.41

Note that the detectability range for IGM at both frequencies for this particular baseline would be insufficient to detect all anomalous gradients specified within the ionospheric threat models (Datta-Barua et al. (2010), Mayer et al. (2009), Yoon et al. (2017)). However, in a real GAST D station, IGM typically utilizes multiple suitable baselines that are meticulously designed to collectively detect all potentially harmful gradients for GBAS.

Furthermore, when we applied an elevation mask of 15°, the threshold values decreased, and the detectability range for both frequencies expanded. This implies that if these values were employed for the monitor, it would become more sensitive and might occasionally trigger false alarms when dealing with very low-elevation satellites. Nevertheless, in a dual or multi-constellation scenario, there could be situations where excluding very low-elevation satellites could enhance the monitor's overall performance. This consideration represents a trade-off parameter and it will be further studied in future work.

3. Airborne Code-Carrier Divergence Monitor

For the airborne CCD analysis, we used data obtained from the user receiver, depicted in red in Figure 1, collected under nominal ionospheric conditions. In this assessment, we computed test statistics, following the methodology outlined in Section II.1, with the distinction of employing time constants (τ in Equations 2 and 3) of 100 seconds instead of 25 seconds.

Figures 8a and 8b present with blue dots the CDF and 1-CDF functions of the normalized test statistic distributions computed

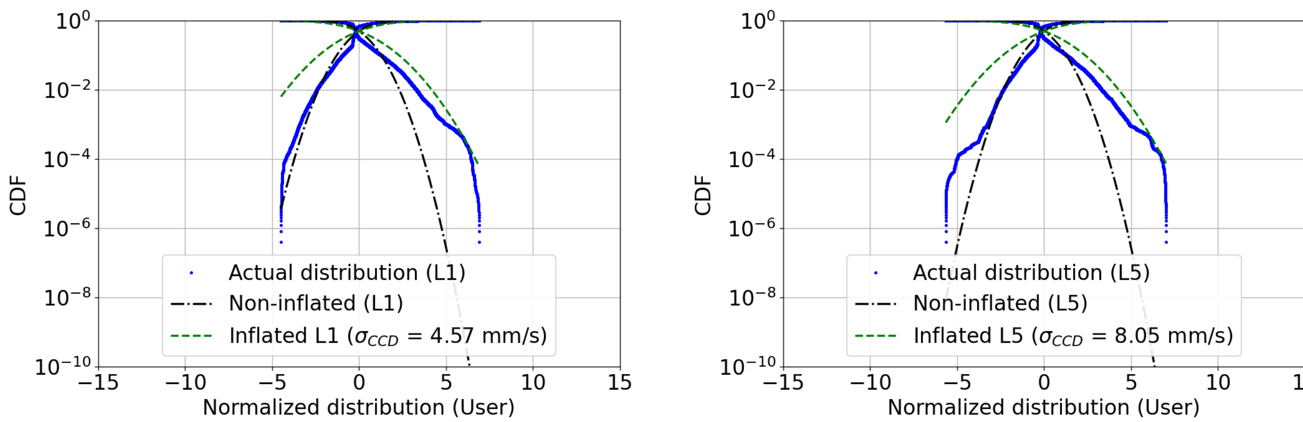

(a) L1/E1 and user receiver.

(b) L5/E5a and user receiver.

Figure 8: Cumulative Distribution Function and its complementary function depicted for the normalized airborne CCD test statistic distributions (blue dots). The black dot-dashed line represents the non-inflated Gaussian distribution and the dashed green line represents the inflated Gaussian distribution.

for the user receiver in the L1/E1 and L5/E5a frequency bands, respectively. In both cases, inflation was needed to protect the tails of the distributions giving as a result inflated standard deviation values of 4.57 mm/s and 8.05 mm/s, respectively.

For the calculation of the detection thresholds, we assumed the same probability of false detection for the airborne CCD and for the ground CCD. The resulting airborne CCD threshold for L1/E1 was 27.01 mm/s, significantly below the value specified in the standards (41.50 mm/s). Therefore, the data collected in Tenerife Norte with the user receiver for L1/E1 and GPS and Galileo also fulfilled the requirements in the standards for GAST D GPS L1.

The resulting airborne CCD threshold for L5/E5a was 47.58 mm/s, which was above the value specified in the standards for GAST D based on GPS L1 (41.50 mm/s). Therefore, we employed this calculated value for subsequent evaluations under active conditions.

Note that the user receiver used in this work was not installed in an aircraft, but instead, on a hill close to the runway at Tenerife Norte Airport. Consequently, it is reasonable to anticipate differences between the results obtained in this study and the corresponding results obtained from receivers installed on aircraft. These differences can come from variations in receiver parameters, potential multipath reflections on the aircraft's airframe, and the use of different antenna types.

4. Dual-Solution Ionospheric Gradient Monitoring Algorithm

For the DSIGMA analysis, we also utilized data obtained from the user receiver, depicted in red in Figure 1, collected under nominal ionospheric conditions. In this assessment, we computed the test statistics following Equation 9.

Figures 9a and 9b present with blue dots the CDF and 1-CDF functions of the normalized test statistic distributions computed for the user receiver in the L1/E1 and L5/E5a frequency bands, respectively. In both cases, inflation was needed to protect the tails of the distributions, giving as a result inflated standard deviation values of 0.158 meters and 0.274 meters, respectively.

By applying the probability of false detection of $1 \cdot 10^{-7}$ specified in Pullen et al. (2017), the resulting DSIGMA threshold for L1/E1 was 0.886 meters, significantly below the value specified in the standards (0.976 meters). Therefore, the data collected in Tenerife Norte with the user receiver for L1/E1 and GPS and Galileo also fulfilled the requirements in the standards for GAST D DSIGMA monitor.

The resulting DSIGMA threshold for L5/E5a was 1.537 meters, which was above the value specified in the standards for GAST D based on GPS L1 (0.976 meters). Therefore, we employed this calculated value for subsequent evaluations under active conditions.

As mentioned previously, since the user receiver used in this work was not installed in an aircraft, we can expect differences between these results and the results that would be obtained using data from more representative installations on an aircraft.

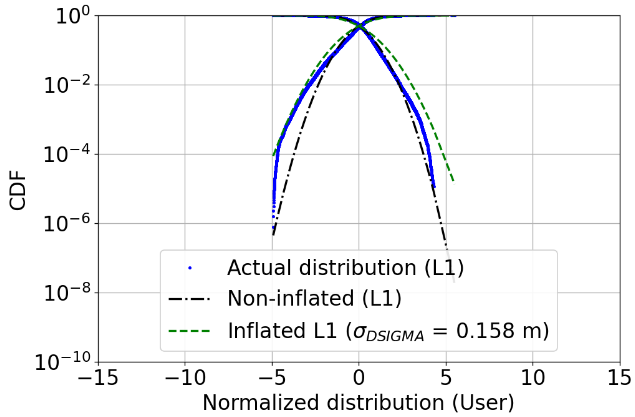

(a) L1/E1 and user receiver.

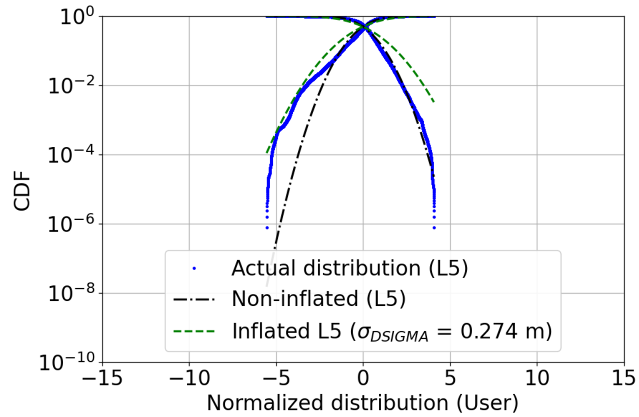

(b) L5/E5a and user receiver.

Figure 9: Cumulative Distribution Function and its complementary function depicted for the normalized DSIGMA test statistic distributions (blue dots) and the user receiver. The black dot-dashed line represents the non-inflated Gaussian distribution and the dashed green line represents the inflated Gaussian distribution.

V. EVALUATION OF THE ADAPTED MONITORS UNDER ACTIVE IONOSPHERIC CONDITIONS

In this section, we evaluate the performance of the monitors adapted in Section IV under active ionospheric conditions.

1. Ground Code-Carrier Divergence Monitor

Figures 10a and 10b show the absolute value of the CCD test statistics calculated for ground reference receiver RX1 on L1/E1 and L5/E5a frequencies, respectively, along with the corresponding thresholds derived in Section IV.1. During daytime (approximately between 07:30 and 18:00), the monitor triggered only once on L1/E1 and a few times on L5/E5a. These triggers were not attributed to slant nominal ionospheric delays but rather to undetected cycle slips, as we employed a basic cycle slip detector in our processing. If one or more cycle slip detectors similar to those implemented in real GBAS ground stations would have been used instead, these triggers would not be present in the plots. The test statistics computed for several satellites presented also upward trends that were close to the threshold values but did not exceed them. These test statistic values corresponded to low elevation satellites, which typically experience a higher ionospheric delay than the high elevation satellites because the path of the signal through the ionosphere is longer.

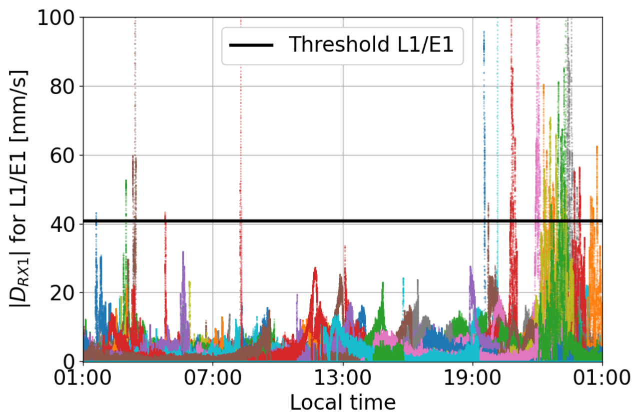

(a) L1/E1 and ground reference receiver RX1.

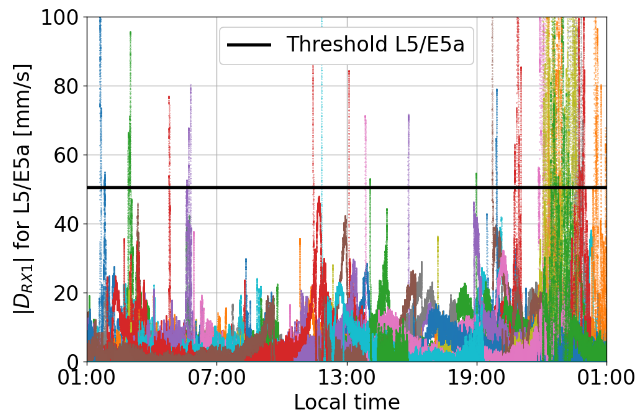

(b) L5/E5a and ground reference receiver RX1.

Figure 10: CCD test statistics in absolute value for L1/E1 and L5/E5a and reference receiver RX1 computed under active ionospheric conditions. The black continuous line represents the threshold.

During evening and nighttime hours (between 18:00 and 07:30 approximately), we observed that the monitoring threshold was frequently exceeded for many satellites for both L1/E1 and L5/E5a. These triggers were a result of scintillation affecting these specific satellites. The minor irregularities in Figure 2b went undetected by both of the monitors implemented on L1/E1 and

L5/E5a, primarily because they are small, and the test statistics did not increase sufficiently to exceed the thresholds. However, we conducted a thorough assessment, and our findings indicated that the observed small irregularities do not present any significant threat to GBAS integrity.

The results for the CCD test statistics computed for the other two ground receivers, RX2 and RX3, were similar. Consequently, we can conclude that the thresholds derived in Section IV were suitable to minimize false alarms while being able to detect active ionospheric conditions.

2. Ground Ionospheric Gradient Monitor

Figure 11a shows the IGM test statistics computed for the L1/E1 frequency band and the data collected at Tenerife Norte Airport during the active ionospheric day. The corresponding threshold (positive and negative values represented as continuous black lines) is the one computed in Section II.2, using the nominal data and applying an elevation mask of $5°$. The calculation of the test statistic follows Equation 5, with the additional step of dividing by the 0.2 km baseline to derive the slope of the gradient in units of millimeters per kilometer (mm/km). As can be observed, the test statistics reached large values and it seemed like there were many anomalous ionospheric gradients that were detected. However, these high gradient estimations were not indicative of actual spatial gradients but rather arose from the effects of scintillation. The reason for this phenomenon is that we did not utilize the output of the ground CCD monitors from RX1 and RX2, which already identified satellites affected by heavy scintillation, as inputs for the IGM. This approach was intentionally chosen to run both monitors in parallel, allowing the evaluation of the IGM's capability to independently detect scintillation events.

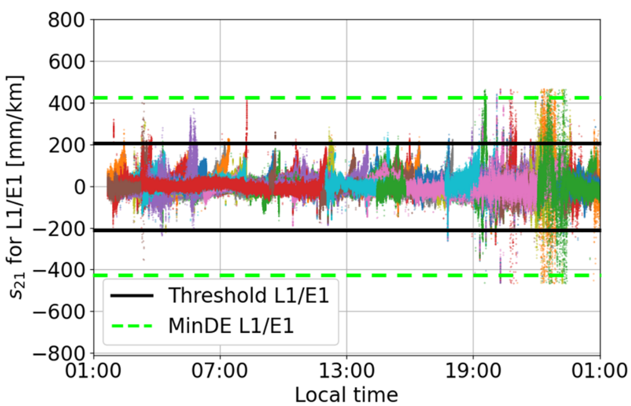

(a) L1/E1 and $5°$ elevation mask.

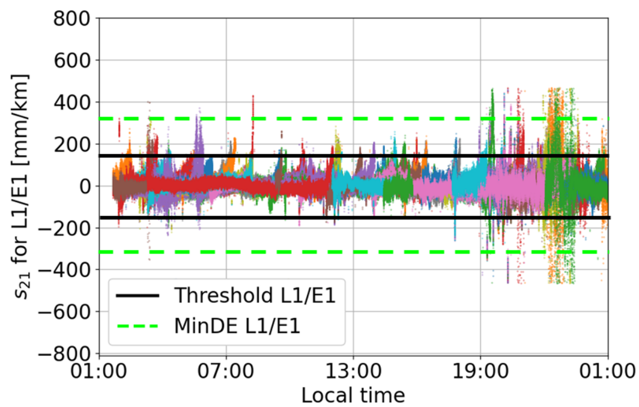

(b) L1/E1 and $15°$ elevation mask.

Figure 11: IGM test statistics computed for L1/E1 using data collected under active ionospheric conditions and thresholds derived with different elevation masks.

Furthermore, the test statistics presented a discontinuity, jumping from 475.73 mm/km to -475.73 mm/km. This phenomenon is a result of the fixed values dictated by the wavelength of L1/E1 (19.05 cm) and the baseline length (0.2 km). Consequently, if the gradient's magnitude exceeds this value (e.g., 500 mm/km), the resulting slope estimate will have a value of -451.46 mm/km. This particularity of the monitor can lead to situations where gradients exceeding a certain value appear indistinguishable from nominal conditions due to this effect (e.g., 800 mm/km becomes -151.46 mm/km and falls within the range of positive and negative threshold values depicted as continuous black lines, 204.14 mm/km and -204.14 mm/kmm, which means that this large gradient would be undetected). Typically, in an operational GAST D ground station, multiple baselines for IGM would be employed to cover the entire range of anomalously large ionospheric gradient values within the ionospheric threat model. In any case, the detection thresholds effectively identified satellites affected by scintillation, as well as two of the satellites affected by minor ionospheric irregularities during nighttime. However, during daytime hours, the monitoring thresholds, despite being computed with all nominal data from satellites above $5°$ of elevation, triggered false alarms for low elevation satellites that presented significantly higher slant ionospheric delays than satellites at mid or high elevations. This implies that a greater amount of nominal data should be used in the threshold derivation to prevent these triggers, but this could also imply an even smaller detection window.

The green lines in Figure 11a represent the values of gradient slopes between the minimum detectable error (425.25 mm/km) and the maximum detectable error (527.25 mm/km, which translates to -425.25 mm/km) that can be detected with this baseline, all with a probability of detection of $1 - P_{MD}$. As can be observed, the space between the green lines and the point where the test statistics jump (both in the positive and the negative parts of the plot) is narrow. This indicates that IGM may not have good detectability when applying a $5°$ elevation mask for the data recorded on the L1/E1 frequency band in Tenerife Norte Airport.

Figure 11b shows once again the IGM test statistics for all satellites above a 5° elevation mask for L1/E1. However, this time, we compared them with the thresholds, minimum detectable errors and maximum detectable errors computed using nominal data from satellites above 15° of elevation. Consequently, the value for the threshold was lower and IGM triggered more false alarms than in the previous case. This could mean that one or more low elevation satellites might be excluded from time to time from the computation of the pseudorange corrections if this elevation mask is used. However, this may be a desired outcome since in certain scenarios, excluding one low elevation satellite might be preferred, especially in multi-constellation scenarios where optimizing the monitor's performance (widening the detectable area between the minimum and the maximum detectable error) for a particular baseline can be advantageous. This is a design parameter and trade-off that needs further investigation in future studies.

Figures 12a and 12b show the IGM test statistics computed using data collected at Tenerife Norte Airport on the L5/E5a frequency during the active ionospheric day and using a 5° elevation mask. The corresponding thresholds (positive and negative values represented as continuous black lines) are the ones computed in Section IV.2, using the nominal data and applying elevation masks of 5° and 15°, respectively. The values for the minimum detectable errors and the maximum detectable errors are shown as green dashed lines for both elevation masks and their specific values can be found in Table 1.

As can be observed, the test statistics for L5/E5a reached a higher maximum value compared to the test statistics for L1/E1 (637.07 mm/km instead of 475.73 mm/km). This difference arose from the longer wavelength associated with L5/E5a (25.48 cm instead of 19.05 cm). Coupled with the fact that the maximum detectable errors are also higher due to wavelength dependency, the detectability window for L5/E5a is significantly larger than that for L1/E1.

As for L1/E1, these threshold values successfully identified all satellites affected by scintillation and two of the minor irregularities. However, the threshold values for L5/E5a also triggered false alarms during the daytime applying both elevation masks. This would lead to the occasional exclusion of low elevation satellites, particularly when applying a 15° elevation mask, but as mentioned previously, this might be preferred in multi-constellation scenarios to enhance the overall performance of the IGM for specific baselines. Furthermore, employing a 15° elevation mask also increased significantly the detectability window for the monitor implemented in the L5/E5a frequency band.

In short, the IGM monitor for L5/E5a demonstrated the capability to detect a greater range of gradient slopes than the IGM for L1/E1. This is reinforced by the fact that, typically, anomalous ionospheric gradients on L5/E5a are assumed to be 1.8 times the magnitude of the anomalous ionospheric gradients on L1/E1 due to the frequency scaling factor. Consequently, even with higher threshold values, the IGM implemented for L5/E5a may respond as effectively, if not more so, than the IGM implemented for L1/E1.

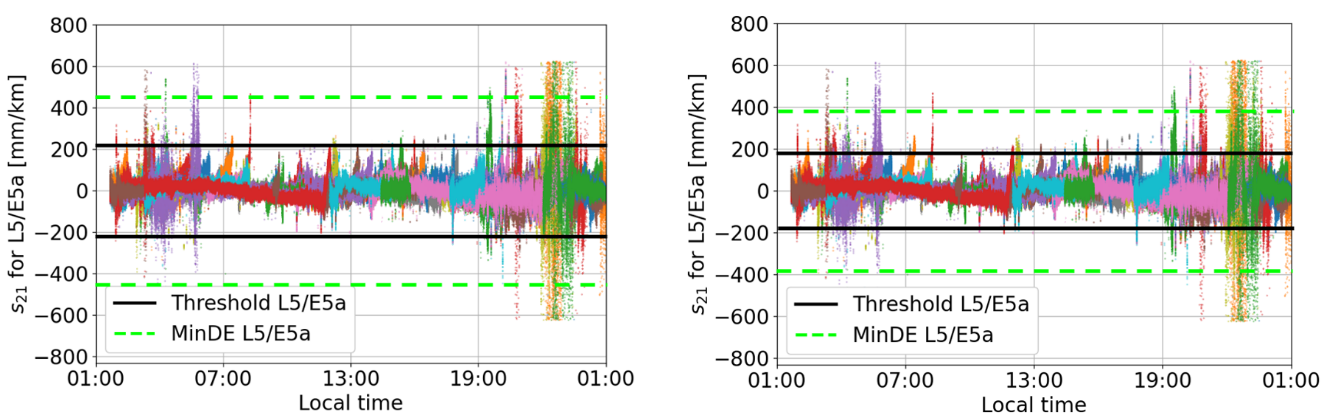

(a) L5/E5a and 5° elevation mask.

(b) L5/E5a and 15° elevation mask.

Figure 12: IGM test statistics computed for L5/E5a using data collected under active ionospheric conditions and thresholds derived with different elevation masks.

3. Airborne Code-Carrier Divergence Monitor

Figures 13a and 13b show the airborne CCD test statistics in absolute value calculated for the user receiver and L1/E1 and L5/E5a, respectively, and the corresponding thresholds derived in Section IV.3. As can be observed, during the daytime hours (between 07:30 and 18:00 approximately), there were a few triggers for the airborne CCD on L1/E1 and only one trigger for L5/E5a. These triggers were again due to undetected cycle slips. Therefore, we can conclude that the threshold values were well derived from the probability of false alert point of view.

During the nighttime (between 18:00 and 07:30 approximately), we can see that the monitoring thresholds were exceeded many times for many satellites in both cases. Those triggers came from the scintillation affecting those specific satellites. The small irregularities present in Figure 2b were not detected by any of the monitors implemented on L1/E1 and L5/E5a because they were very small and the test statistics did not increase sufficiently to exceed the thresholds. However, as previously mentioned, these small irregularities did not present any significant threat to GBAS integrity. Therefore, we can conclude that the derived thresholds in Section IV.3 are also applicable when the ionosphere is in an active state.

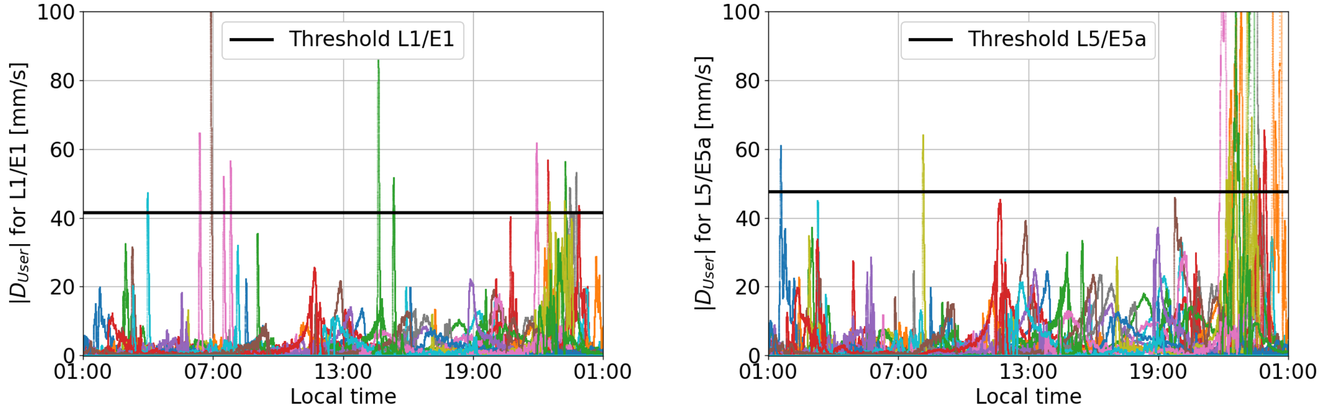

(a) L1/E1 and user receiver.

(b) L5/E5a and user receiver.

Figure 13: Airborne CCD test statistics in absolute value for L1/E1 and L5/E5a and the user receiver computed using data under active ionospheric conditions. The black continuous line represents the threshold.

4. Dual Solution Ionospheric Gradient Monitoring Algorithm

Figures 14a and 14b show the DSIGMA test statistics in absolute value calculated for the user receiver and the L1/E1 and L5/E5a frequency bands, and the corresponding thresholds.

As can be observed, none of the DSIGMA monitors for L1/E1 and L5/E5a triggered during high ionospheric activity. The principal factor contributing to this outcome was that the cycle slip detectors triggered a re-initialization of the single-frequency smoothing filters, effectively mitigating most of the scintillation effects.

Furthermore, the minor irregularities observed during these conditions did also not trigger DSIGMA on any of the frequencies. As mentioned previously, subsequent investigation confirmed that these irregularities do not pose any harm to the integrity of the position solution computed by GBAS.

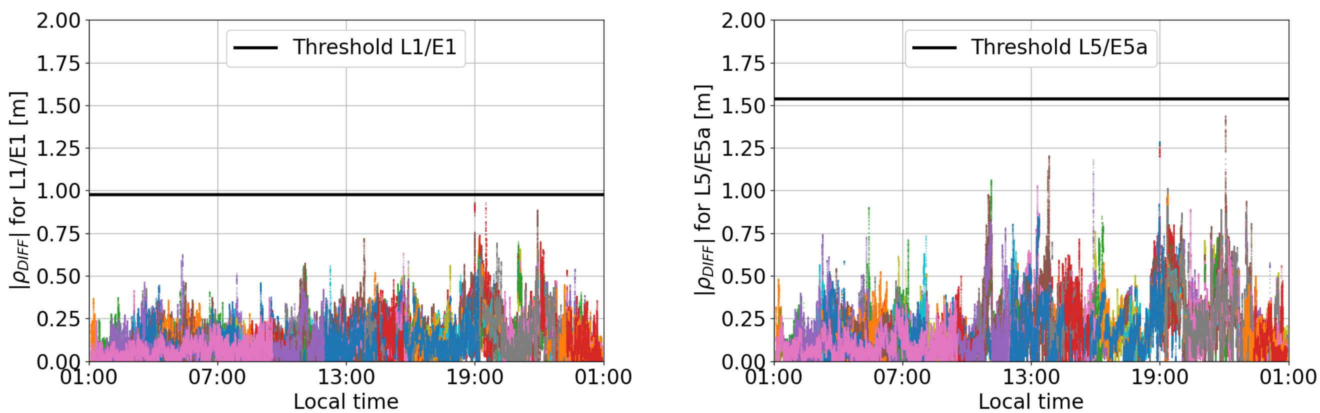

(a) L1/E1 and user receiver.

(b) L5/E5a and user receiver.

Figure 14: DSIGMA test statistics in absolute value for L1/E1 and L5/E5a and the user receiver computed using data under active ionospheric conditions. The black continuous line represents the threshold.

VI. CONCLUSIONS AND FUTURE WORK

This paper presents an evaluation of the performance of the GAST D equivalent mode implemented for the L5/E5a frequency band, under both nominal and active ionospheric conditions.

Under nominal conditions, the results demonstrated that the monitoring thresholds specified in the existing GAST D standards were applicable and effective for data collected on the L1/E1 frequency band for both GPS and Galileo at Tenerife Norte Airport. However, when applied to the L5/E5a frequency band, these thresholds proved inadequate, potentially leading to an excessive number of false alarms. To address this, we adjusted the thresholds for all monitors by considering false detection probabilities and missed detection probabilities from the current GAST D standards, and the inflated standard deviations computed from the distributions of test statistics calculated using L5/E5a data.

Under active ionospheric conditions, the adapted thresholds for ground CCD, airborne CCD, and DSIGMA exhibited robust performance in detecting high ionospheric activity. Conversely, the IGM L1/E1 and L5/E5a thresholds for both elevation masks at 5° and 15°, were found to be relatively low, potentially triggering false alarms. This could lead to the exclusion of one or more low elevation satellites from the computation of pseudorange corrections in nominal conditions. IGM thresholds could be increased if derived with more nominal data, but this would also lead to smaller detectability areas between the minimum detectable errors and the maximum detectable errors. Therefore, there is a trade-off between reducing the threshold value, excluding one or more low elevation satellites and increasing the detectabilitay area of IGM for a certain baseline. Notably, the IGM thresholds proved effective in detecting scintillation and even two of the minor ionospheric irregularities, demonstrating greater sensitivity compared to other monitors. Regardless, the non-detection of small irregularities did not impact GBAS integrity. Furthermore, the range of detectable gradient slopes for IGM for L5/E5a was larger than for L1/E1 as it depends on the wavelength, which is larger for L5/E5a than for L1/E1.

Future work will focus on the characterization of MLA errors to optimize the performance of the IGM for both frequencies. Furthermore, we will evaluate the performance of the "L5/E5a GAST D equivalent mode" in simulation and with more real measurements to obtain the position errors and assess if CAT III performance requirements can be met or alternative or additional monitors might be needed to provide sufficient integrity.

ACKNOWLEDGEMENTS

The authors would like to thank Enaire, INDRA Satnav, and INDRA Navia for providing the data from the GBAS installation in Tenerife in the frame of the European project SESAR 2020 PJ14 W2 WP9 Sol79b.

REFERENCES

Caamano, M., Gerbeth, D., Sato, H., Circiu, M.-S., and Felux, M. (2023). Performance Evaluation of the Ionospheric Threat Mitigation Strategies in Dual-Frequency Multi-Constellation GBAS. In *2023 IEEE/ION Position, Location and Navigation Symposium (PLANS)*, pages 196–207. IEEE.

Datta-Barua, S., Lee, J., Pullen, S., Luo, M., Ene, A., Qiu, D., Zhang, G., and Enge, P. (2010). Ionospheric threat parameterization for local area Global-Positioning-System-based aircraft landing systems. *Journal of Aircraft*, 47(4):1141–1151. doi: 10.2514/1.46719.

Durba, P. (2018). WP27 - High level concept and modes for DFMC GBAS. Technical report, ICAO NSP - Joint Working Groups.

Gerbeth, D., Caamano, M., Circiu, M.-S., and Felux, M. (2022). Airborne Ionospheric Gradient Monitoring for Dual-Frequency GBAS. In *Proceedings of the 2022 International Technical Meeting of The Institute of Navigation*, pages 1110–1122.

Gerbeth, D., Circiu, M.-S., Caamano, M., and Felux, M. (2016). Nominal Performance of Future Dual Frequency Dual Constellation GBAS. *International Journal of Aerospace Engineering*, 2016:1–20.

Khanafseh, S., Pullen, S., and Warburton, J. (2012). Carrier Phase Ionospheric Gradient Ground Monitor for GBAS with Experimental Validation. *NAVIGATION*, 59(1):51–60. doi: 10.1002/navi.3.

Mayer, C., Belabbas, B., Jakowski, N., Meurer, M., and Dunkel, W. (2009). Ionosphere Threat Space Model Assessment for GBAS. *Proceedings of the 22nd International Technical Meeting of the Satellite Division of the Institute of Navigation (ION GNSS 2009)*, pages 1091–1099.

Murphy, T., Harris, M., Balvedi, G., McGraw, G., Wichgers, J., Lavik, L., Topland, M., Tuffaha, M., and Saito, S. (2022). Ionospheric Gradient Monitoring for Dual Frequency Multi-Constellation GBAS. In *Proceedings of the 2022 International Technical Meeting of The Institute of Navigation*, pages 1075–1097.

Murphy, T., Harris, M., McGraw, G., Wichgers, J., Lavik, L., Topland, M., Tuffaha, M., and Saito, S. (2021). Alternative Architecture for Dual Frequency Multi-Constellation GBAS. In *Proceedings of the 34th International Technical Meeting of the Satellite Division of The Institute of Navigation (ION GNSS+ 2021)*, pages 1334–1374.

Pullen, S., Cassell, R., Johnson, B., Brenner, M., Weed, D., Cypriano, L., Topland, M., Stakkeland, M., Pervan, B., Harris, M., Saito, S., Lee, J., Clark, B., Beauchamp, S., and Dennis, J. (2017). Impact of Ionospheric Anomalies on GBAS GAST D Service and Validation of Relevant ICAO SARPs Requirements. *Proceedings of the 30th International Technical Meeting of the Satellite Division of The Institute of Navigation (ION GNSS+ 2017)*, pages 2085–2105.

Pullen, S., Park, Y. S., and Enge, P. (2009). Impact and mitigation of ionospheric anomalies on ground-based augmentation of GNSS. *Radio Science*, 44.

Radio Technical Commission for Aeronautics (2017). DO-253D, Minimum Operational Performance Standards for GPS Local Area Augmentation System Airborne Equipment. Technical report.

Sokolova, N., Morrison, A., and Diez, A. (2022). Characterization of the GNSS RFI Threat to DFMC GBAS Signal Bands. *Sensors*, 22(22):8587.

Yoon, M., Lee, J., Pullen, S., Gillespie, J., Mathur, N., Cole, R., de Souza, J., Doherty, P., and Pradipta, R. (2017). Equatorial Plasma Bubble Threat Parameterization to Support GBAS Operations in the Brazilian Region. *NAVIGATION*, 64(3):309–321.